Materials Advances

ROYAL SOCIETY OF CHEMISTRY

PAPER

View Article Online
View Journal | View Issue

Cite this: *Mater. Adv.*, 2025, **6**, 1899

Investigating the potential of a self-healing semiconducting supramolecular Mg(II)-metallohydrogel in non-volatile memory design and its therapeutic properties towards bacteria infected wound healing†

Subhendu Dhibar,‡*[a] Arpita Roy,‡[b] Priyanka Das,‡[c] Tuhin Sarkar,[c] Mitrabrata Goswami,[c] Sangita Some,[a] Kripasindhu Karmakar,[a] Pradip Ruidas,[d] Subham Bhattacharjee,[d] Timothy O. Ajiboye,[e] Anindya Sundar Ray,[f] Keka Sarkar,*[c] Soumya Jyoti Ray*[b] and Bidyut Saha*[a]

A swift and effective technique was employed to fabricate a novel supramolecular metallohydrogel, named Mg@5AP, by incorporating Mg(II) ions. This groundbreaking gel utilized 5-amino-1-pentanol as a low molecular weight gelator, formulated in an aqueous solution at room temperature. Mechanical robustness was assessed through rheological analysis, affirming the resilience of Mg@5AP under various mechanical strains and angular frequencies. Notably, the metallohydrogel displayed thixotropic properties, indicating its ability to self-repair. Structural characterization revealed a distinct network of rectangular, mixed flake rod-like structures within Mg@5AP, as observed through scanning and transmission electron microscopy (FESEM and TEM). Elemental mapping using energy-dispersive X-ray (EDX) analysis confirmed the presence of key chemical components. Further insights into its formation were obtained *via* Fourier-transform infrared (FT-IR) spectroscopy. In this investigation, Schottky diode structures in a metal–semiconductor–metal arrangement were fabricated using the magnesium(II) metallohydrogel (Mg@5AP) to explore its charge transport behavior. Additionally, a resistive random access memory (RRAM) device was fabricated from Mg@5AP, showcasing bipolar resistive switching at room temperature. A detailed observation of the switching mechanism, involving the formation and disruption of conduction filaments, explained the resistive switching process. The RRAM device exhibited exceptional performance with a high ON/OFF ratio of approximately 120 and impressive endurance, surpassing 5000 switching cycles. This durability suggests the suitability of these devices without any electrical degradation. Furthermore, Mg@5AP demonstrated significant inhibitory activity against drug-resistant Klebsiella pneumonia strain and its biofilm formation. The minimum inhibitory concentration (MIC) was determined to be 3 mg mL^{-1} when dissolved in 1% dimethyl sulfoxide (DMSO). An MTT assay revealed a 60% inhibition of biofilm formation at a concentration of 1 mg mL^{-1} of Mg@5AP in 1% DMSO. Moreover, in a mouse excisional wound model, Mg@5AP played a pivotal role in preventing postoperative wound infections and promoting wound healing.

Received 13th December 2024,
Accepted 10th February 2025

DOI: 10.1039/d4ma01238k

rsc.li/materials-advances

[a] *Colloid Chemistry Laboratory, Department of Chemistry, The University of Burdwan, Golapbag, Burdwan-713104, West Bengal, India. E-mail: sdhibar@scholar.buruniv.ac.in, bsaha@chem.buruniv.ac.in; Tel: +91 7001575909, +91 9476341691*
[b] *Department of Physics, Indian Institute of Technology Patna, Bihar-801106, India. E-mail: ray@iitp.ac.in*
[c] *Department of Microbiology, University of Kalyani, Kalyani-741235, India. E-mail: keka@klyuniv.ac.in*
[d] *Department of Chemistry, Kazi Nazrul University, Asansol, 713303, West Bengal, India*
[e] *Department of Chemistry, University of the Free State, Bloemfontein, 9301, South Africa*
[f] *Ethnopharmacology Laboratory, Department of Biological Sciences and Microbiology, Biswa Bangla Biswabidyalay (University), BolpurShibpur, Birbhum, PIN No. 731204, West Bengal, India*

† Electronic supplementary information (ESI) available. See DOI: https://doi.org/10.1039/d4ma01238k

‡ SD, AR and PD should be treated as joint first authors.

1. Introduction

Supramolecular gels are an intriguing and promising area of study in supramolecular chemistry. These gels are viscoelastic solids, composed of a solvent intertwined with an elastic, cross-linked network. The self-assembly of molecules in these gels leads to the formation of intricate three-dimensional structures. The gels appear solid due to the containment of liquid within and its adherence to the extensive surface area of a 3D-solid matrix.[1,2] The formation of these networks relies on various non-covalent interactions, such as hydrophobic contacts, van der Waals forces, cation$\cdots\pi$, anion$\cdots\pi$, $\pi\cdots\pi$, hydrogen bonding, dipole–dipole, ion–ion, and dipole–dipole interactions, which have been crucial in their development.[3,4] By harnessing supramolecular phenomena, researchers have been able to create three-dimensional soft gel scaffolds.

Supramolecular gels often involve low molecular weight gelators (LMWGs) as key components. These LMWGs are small molecules with a molecular weight of 3000 or less that possess the ability to self-assemble through non-covalent interactions, forming a three-dimensional network that traps the solvent and gives rise to the gel's viscoelastic properties. The advantage of using low molecular weight gelators is that they offer precise control over the gel's properties. By modifying the chemical structure of these small molecules, researchers can tailor the gel's mechanical strength, stability, and responsiveness to external stimuli. This tunability makes supramolecular gels with LMWGs attractive for various applications, including drug delivery, tissue engineering, sensors, molecular electronics, wound healing and templating self-assembly morphology.[5–11] Moreover, their reversible gelation behavior allows for the gel to form and dissolve based on environmental changes, making them dynamic and adaptable materials.[5–7] A wide range of low-molecular-weight gelators have been acknowledged in the literature as essential components in the formation of supramolecular gels. These gelators include diverse compounds such as amino acids,[12,13] peptides,[14,15] amides,[16,17] carbohydrates,[18] cholesterol,[19,20] alkenes,[21] bile acids,[22] saccharides,[23] sugars,[24] and urea derivatives.[25] The self-assembly of these molecules gives rise to three-dimensional networks that define supramolecular gels.

Appropriate solvent selection is crucial for the successful gelation of supramolecular gels. These gels can be categorized into hydrogels and organogels, depending on the solvent used. To facilitate the self-assembly of LMWGs and the formation of supramolecular gel networks, a range of potent solvents are employed, such as water,[26] acetone,[27] alcohol,[28] tetrahydrofuran,[29] toluene,[30] carbon tetrachloride,[31] dimethyl sulfoxide,[32] and dimethylformamide,[33] among others. Careful selection of the appropriate solvent allows researchers to control the gelation process and tailor the properties of the resulting gels, making them suitable for various applications.

Recently, in the field of supramolecular chemistry there has been growing interest in metallogels, primarily formed due to metal–ligand interactions.[34] Supramolecular metallogel is a gel formed through self-assembly *via* metal–ligand interactions in supramolecular chemistry. In this type of gel, metal ions or metal complexes play a crucial role in the gelation process, binding with ligands to form a three-dimensional network structure. The resulting gel exhibits unique properties and functionalities, making it a subject of increasing interest in various fields, including materials science, catalysis, and biomedical applications.[35–37] The ability to tailor the metal–ligand interactions allows for the design of supramolecular metallogels with specific properties and responsiveness to external stimuli, expanding their potential for innovative applications. Furthermore, these metallogels demonstrate a wide range of properties and functionalities, including conductivity,[38] redox reactivity,[39] catalytic activity,[40] proton conductivity,[41] and magnetic behavior.[42] This versatility allows researchers to explore their potential in various fields, such as in electronic devices,[43] energy storage,[44] catalysis,[36] and biomedical applications.[37] Using water as a solvent in the gelation process enables diverse self-assembly processes, leading to the production of functional gel materials with tunable properties. This versatility in metal–ligand coordination and solvent selection has fueled extensive research and significance in the development of supramolecular metallogels.

In this research, we successfully produced a metallohydrogel named Mg@5AP by combining the magnesium(II) salt and 5-amino-1-pentanol (5AP) ligand under ambient conditions, without the need for organic solvents. This metallohydrogel formation was achieved by directly mixing 5-amino-1-pentanol, a low molecular weight gelator ligand, with magnesium nitrate hexahydrate in an aqueous medium.

On the other hand, resistive switching is a phenomenon where there is a change in resistance between two resistance states like the high resistance state (HRS) and low resistance state (LRS). This means the devices can switch between these two states. Resistive random access memory (RRAM) devices possess remarkable memory capabilities, making them valuable across diverse fields, including non-volatile memory design, and in memory and neuromorphic computing.[45,46] These devices depend on physical phenomena such as vacancy migration and charge carrier trapping to switch between high- and low-resistance states for their operation. Metallohydrogels, as an alternative to oxide materials, offer promising prospects in RRAM design, enabling the development of flexible electronics and metal–semiconductor (MS) junctions.[47–49] Our approach of creating a flexible and functional soft gel scaffold through Mg(II)-metallohydrogel contributes significantly to the advancement of memory devices, particularly in data-centric applications like Internet of Things (IoT) and 5G connectivity. This research and technology has the potential to open up new horizons in the field of memory devices.[35,47,50]

Antibiotic resistance has emerged as a major concern for healthcare professionals, veterinarians, and others involved in infection management. Previously treatable bacteria are now reappearing in drug-resistant forms, complicating treatment and prevention efforts. This challenge is particularly pronounced for pathogens like *Klebsiella pneumoniae* (KP) and *Staphylococcus aureus* (MRSA), which have garnered significant attention due to their public health impact. *Klebsiella pneumoniae* is responsible for a substantial number of Gram-negative infections, encompassing conditions like pneumonia, urinary

tract infections, and surgical wound infections. It can also lead to severe illnesses such as necrotizing pneumonia and liver abscesses. MRSA, on the other hand, causes infections in both community and healthcare settings, ranging from minor skin issues to severe cases like pneumonia and sepsis. Infections caused by these pathogens are associated with high mortality rates, prolonged hospitalizations, and increased healthcare costs. Multidrug-resistant (MDR) and extremely drug-resistant (XDR) strains of these bacteria have become increasingly prevalent. Notably, both KP and MRSA are capable of forming biofilms, complex bacterial communities surrounded by a matrix of polysaccharides, proteins, and DNA. The presence of biofilms enhances resistance to external factors and conventional antibiotics, rendering eradication challenging.

This study also delved into the ability of the synthesized hydrogel, Mg@5AP, to combat bacterial infections and inhibit biofilm formation initiated by KP and MRSA. We examined the antibacterial and anti-biofilm properties of Mg@5AP using an *in vitro* model. To further validate the therapeutic potential of Mg@5AP, we conducted *in-vivo* experiments on Swiss albino rats *via* wound healing assays, infecting them with these two studied bacteria.

2. Experimental

2.1. Materials

Magnesium nitrate hexahydrate (98% reagent grade) was acquired from Sigma-Aldrich, and 5-amino-1-pentanol was obtained from Tokyo Chemical Industry (TCI). Both chemicals were utilized in their as-received state without additional purification. Double-distilled water was consistently used in all experiments.

2.2. Apparatus and measurements

Absorption spectroscopic data were collected using a SHIMADZU UV-3101PC spectrophotometer.

Rheological investigations, which included angular frequency and oscillatory amplitude sweeps, were carried out with a DHR-2 stress-controlled rheometer from TA Instruments.

For capturing FESEM (field emission scanning electron microscopy) images, a Carl Zeiss SUPRA 55VP FESEM instrument was employed, while TEM (transmission electron microscopy) images were obtained using an aberration-corrected FEI Titan Themis operating at 300 kV. Chemical constituent elemental mapping was conducted using a ZEISS EVO 18 microscope.

FT-IR spectroscopic analysis was performed using a JASCO FTIR 4700 spectrometer.

Current–voltage (*I–V*) measurements for devices based on the synthesized metallohydrogel material were conducted at room temperature using a Keithley 2400 sourcemeter, interfaced through Labview.

2.3. Synthesis of magnesium(II)-metallohydrogel (Mg@5AP)

A 500 μL clear aqueous solution containing $Mg(NO_3)_2{\cdot}6H_2O$ (0.256 g, 1 mM) and 500 μL of 5-amino-1-pentanol was rapidly combined within a 5 mL glass vial at room temperature, under normal atmospheric conditions. Following gentle shaking of the vial, a stable white-colored Mg(II)-metallohydrogel (Mg@5AP) was instantly created within 30 seconds (see Fig. 1).

Fig. 1 presents a plausible schematic representation of Mg@5AP, accompanied by an inverted image demonstrating the stability of Mg@5AP. The Minimum Critical Gelation (MGC) of Mg@5AP was determined by varying the metallohydrogel concentrations within the range of 50 mg mL^{-1} to 256 mg mL^{-1}. The successful formation of the Mg@5AP metallohydrogel was achieved at a concentration of 256 mg mL^{-1}, as shown in Fig. 2. Here, we further investigated using different concentrations of 5-amino-1-pentanol (*i.e.* 50 μL, 100 μL, 200 μL, 400 μL and 500 μL) to obtain metallohydrogel formation. Remarkably, gel formation was observed only with 1 mM $Mg(NO_3)_2{\cdot}6H_2O$ salts and 500 μL 5-amino-1-pentanol under the above-mentioned conditions (see the ESI,† Table S1) We have also examined using different magnesium salts (*i.e.* Mg(II)-acetate tetrahydrate, Mg(II)-chloride and Mg(II)-carbonate) to obtain different metallohydrogels. Remarkably, gel formation was observed only with $Mg(NO_3)_2{\cdot}6H_2O$ salts under the above-mentioned condition (see the ESI,† Table S2). The gel-to-sol transition temperature (T_{gel}) of Mg@5AP was found to be 210 °C.

2.4. Agar cup assay for antibacterial activity

Klebsiella (ATCC BAA 1705), a Gram-negative bacteria and MRSA (ATCC 700699), a Gram-positive bacteria were used as the test organisms to assess the antibacterial efficacy of Mg@5AP. Overnight grown fresh cultures of both organisms were transferred separately onto nutrient agar plates supplemented with 1% glucose and 1% sodium chloride. A cooled sterile bacterial spreader was used to evenly distribute the culture broth across the agar surface, after which the plate was placed in a refrigerator at 4 °C for thirty minutes. A loopful of Mg@5AP was placed at the center of a Petri dish, previously inoculated with both microorganisms separately, and cefoxitin

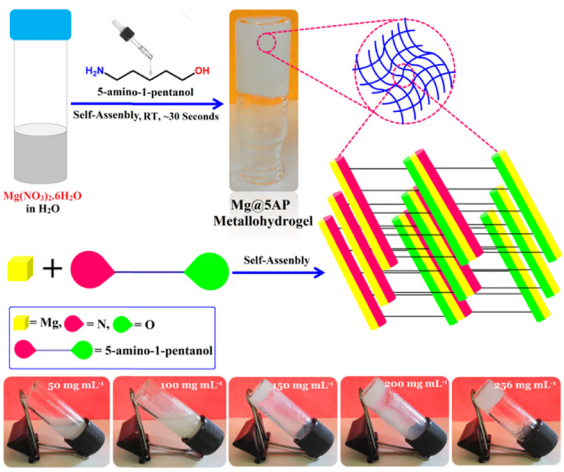

Fig. 1 The process of gelation follows this synthetic procedure, ultimately resulting in the creation of Mg(II)-metallohydrogel (Mg@5AP). This is followed by the presentation of a photographic image and a schematic diagram depicting the resulting Mg@5AP metallohydrogel and exploring the minimum critical gelation (MGC) of Mg(II)-metallohydrogel at a fixed concentration of 256 mg mL^{-1} by varying concentrations.

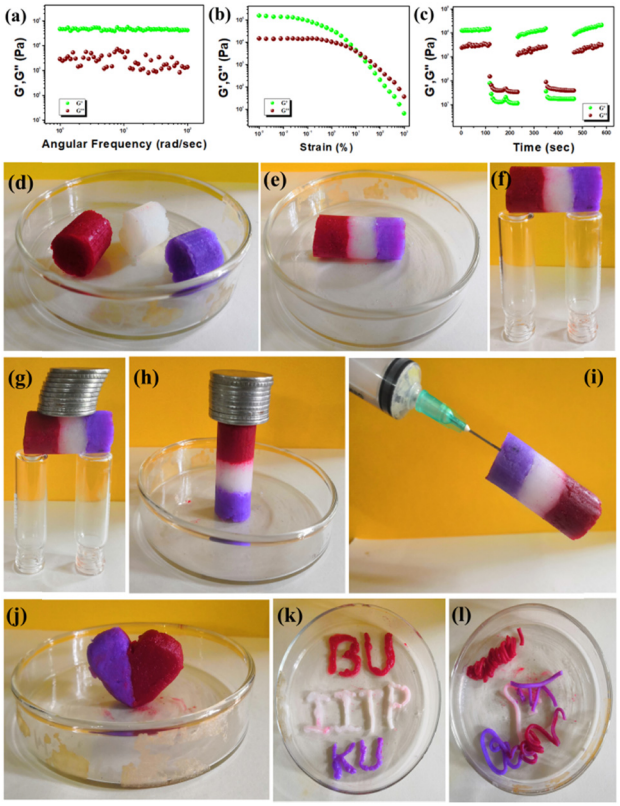

Fig. 2 (a) Plot illustrating the relationship between angular frequency and storage modulus (G') and loss modulus (G'') of the Mg@5AP metallohydrogel; (b) strain-sweep experiments conducted on the Mg@5AP metallohydrogel at a constant frequency of 6.27997 rad s^{-1}; (c) thixotropic measurement performed on the Mg@5AP metallohydrogel, examining its thixotropic behavior; (d)–(f) self-healing and self-supported monolith bridge constructed by cylindrical blocks of Mg@5AP metallohydrogel; (g) and (h) load-bearing properties of the Mg@5AP metallohydrogel made by alternate dye-doped and undoped blocks of gel; (i) alternate arrangement of self-healing Mg@5AP gel against gravity; (j)–(l) self-sustaining nature of Mg@5AP gel: (j) molded into heart shape, (k) used as ink, and (l) noddle shape design formation from Mg@5AP gel.

disks were used as a standard (followed by CLSI23 guideline) at a concentration of 30 μg mL^{-1}, denoted as CX-30. The prepared Petri dishes were then placed in an incubator at 37 °C for 24 hours to observe any appearance of a hollow zone surrounding the Mg@5AP.[51]

2.5. MICs (minimum inhibitory concentrations)

The MICs of Mg@5AP were ascertained against *Klebsiella* and MRSA through the conventional broth microdilution technique. 100 μL of an overnight cultured bacterial cell suspension was added to 3 mL of fresh nutrient broth containing varying concentrations of Mg@5AP in 1% DMSO (v/v), ranging from 100 μg mL^{-1} to 8 mg mL^{-1}. For a positive control set, 1% DMSO (v/v) was used, along with an equivalent volume of bacterial inoculum within the medium. These test tubes were then placed within a shaker incubator at 160 rpm and 37 °C for 24 hours. Following this incubation period, the percentage of growth responses was evaluated by measuring the optical density (OD) value at 600 nm using a spectrophotometer.[52]

2.6. Scanning electron microscopy (SEM)

A 100 μl bacterial suspension of overnight grown MRSA and *Klebsiella* cultures was added separately to 2 mL of fresh nutrient broth and treated with 6 mg mL^{-1} Mg@5AP, dissolved in 1% DMSO. The mixture was then incubated at 160 rpm and 37 °C for 24 hours. On the subsequent day, 1 mL of the treated broth was taken into a 1.5 mL micro-centrifuge tube and centrifuged at 10 000 rpm for 5 minutes. The pellet was thoroughly washed thrice with 1× PBS and finally dissolved in 100 μl of 1× PBS. A volume of 5 μl suspension was applied onto 12 mm coverslips and allowed to dry. For fixation, 10 μl of 2.5% glutaraldehyde was added, and the coverslips were stored in a dark environment at 4 °C overnight. On the following day, the coverslips underwent a series of ethanol washes with varying concentrations ranging from 30% to 100% and were then placed within a desiccator to facilitate complete drying.[53]

2.7. Biofilm inhibition assay

Crystal violet (CV) analysis was used to measure biofilm inhibition. This method quantifies the mass of the total biofilm by calculating how well the dye adheres to both viable and non-viable bacterial cells and extracellular polymeric substances (EPS). In a 96 well plate 1×10^6 cells were grown in each well and kept for a 24-hour incubation period at 37 °C. To get rid of loosely bound bacteria, the 24-hour-grown biofilms were gently washed twice with phosphate-buffered saline (1× PBS, pH = 7.4). Following a 24-hour incubation period at 37 °C, the formed biofilms were subsequently exposed to Mg@5AP, dissolved in 1% DMSO at various doses (1, 5, 10, and 20 mg mL^{-1}), and incubated for 24 h. After treatment, the biofilms were washed with 1× PBS to remove any remaining solution. Once the biofilms had been stained for 20 minutes at room temperature, 100 μL of a 1% (w/v) crystal violet solution was added to each well. The biofilms underwent 1× PBS washes three times after being stained in order to remove any remaining dye. Following this, 150 μL of 70% ethanol was added to each well, and the absorbance was measured at 595 nm using a microplate reader.[54] The percentage of biofilm inhibition is calculated using the following formula: % biofilm inhibition = [(OD595 of control − OD595 of treated biofilm)/OD595 of control] × 100.

2.8. Confocal microscopy

MRSA and *Klebsiella* (at a concentration of 10^7 CFU mL^{-1}) were grown on 6-well Petri plates with 12 mm coverslips to investigate the effect of Mg@5AP on the development of bacterial biofilm on glass surfaces. A sub-MIC dosage of Mg@5AP and one positive control using 1% DMSO were added to the culture medium of 1% glucose and 1% sodium chloride nutritional broth. The Petri plate was then kept in a static condition for 48 hours in an incubator at 37 °C. After the incubation period, the planktonic cell-containing liquid was carefully washed without disrupting the biofilm that had developed on the coverslips. Cells that were loosely bound were removed with a gentle rinse in sterile 1× PBS. The samples were then fixed for 60 minutes at room temperature with 2.5% glutaraldehyde (v/v) and then

washed with sterile 1× PBS. After fixation, the adhered biofilm on the coverslips was stained with acridine orange at a concentration of 10 μg mL^{-1} for 30 minutes in the dark at room temperature. This was followed by washes with sterile 1× PBS twice to remove excess dye. Finally, the coverslips were placed on clean glass slides using a DPX mountant.[55]

2.9. *In vivo* wound healing assay

All procedures were carried out in accordance with the guidelines published by the University of Kalyani's IAEC (892/GO/Re/S/01/CPCSEA). Following an evaluation, the Animal Ethics Committee (idea Number: KU/29.03.23/04) approved the idea. 6–10 week old male mice (Swiss albino) were obtained from the State Centre for Laboratory Animal Breeding, Buddha Park, Kalyani, Nadia, W.B., India. The animals were housed under good conditions kept at 25 ± 1 °C and 15–25% humidity was maintained with a standard light and dark cycle (12 hour). In separate cages, the mice were also maintained with fresh water and proper food. To conduct the tests, we separated the animals into groups and subjected them to various treatments in accordance with the experimental protocol. After anaesthesia with ketamine and xylazine, the skin was removed with a biopsy punch kit (3 mm). Following skin excision, the wound area was cleaned with PBS solution, and the animals were monitored until they recovered from the anaesthetic effect.[56] The experiment was conducted through division of animals into five groups: For Group 1, only the wound was created and considered as the control. Group 2 had the KP contaminated wound and Group 3 had the MRSA contaminated wound. Group 4 mice were treated with the Mg@5AP gel containing a KP infected wound, and the mice with the MRSA infected wound, but treated with the Mg@5AP gel were considered as Group 5. Following treatment, the animals were monitored from time to time and the photographs were taken accordingly.[56]

2.10. HE Staining

Skin tissue samples of the wound area were collected and fixed in 10% neutral buffer formalin and subsequently embedded in paraffin for the preparation of pathological slides. Following haematoxylin and eosin (H&E) staining, the histological images were examined using a brightfield microscope.[57]

2.11. Haemolysis assay

Haemolysis assay was evaluated with fresh goat blood and stabilized with Heparin.[58] 2 mL of whole blood sample was added to 4 mL phosphate-buffered saline and then centrifugated at 10 000 rpm for 5 min to isolate red blood cells (RBCs). The RBCs were further washed 3 times with 1 mL of PBS and finally diluted to 10 mL with PBS. 0.2 mL of diluted RBC suspension was exposed to 0.8 mL of the Mg@5AP – PBS suspension at concentrations of 3, 6 & 12 mg mL^{-1}. A positive control set was prepared with Triton X (to determine lysis) and a negative control set with PBS. The samples were incubated at 37 °C for 60 min and centrifuged for 5 min at 10 000 rpm before taking the photograph.

2.12. Cytotoxicity assay [MTT assay]

The cytotoxicity of the Mg@5AP compound was evaluated using the MTT assay.[59] HEK293T (human embryonic kidney cells) cells (1×10^4 cells per mL) were seeded into 96-well plates with 100 μL of DMEM and incubated for 24 hours. Following this, the cells were treated with varying concentrations of Mg@5AP (3, 6, 9, and 12 mg mL^{-1}) in 100 μL of media and incubated for an additional 48 hours. After 48-hours of incubation, 10 μL of MTT reagent (5 mg mL^{-1}) was added to each well. The plates were then incubated at 37 °C for 4 hours, after which the MTT reagent was removed. Dimethyl sulfoxide (DMSO) (200 μL) was added to each well, and absorbance was measured at a wavelength of 595 nm using an ELISA reader. The IC50 value was determined, and all assays were conducted in triplicate, with the results expressed as mean ± SD.

3. Results and discussion

3.1 Rheological analysis and self-healing performance of Mg@5AP metallohydrogel

Rheological experiments showed the viscoelastic semi-solid characteristics of the Mg(II)-metallohydrogel. The storage modulus (G') and loss modulus (G'') were measured to gauge the gel's behavior. In the viscoelastic domain, the system stores energy, denoted by G' as $(\sigma_0/\gamma_0)\cos(\delta)$, while dissipating energy due to oscillatory stress, represented by G'' as $(\sigma_0/\gamma_0)\sin(\delta)$. To categorize the material as a gel, it must meet the condition $G'(\omega) > G''(\omega)$, where $G'(\omega)$ is approximately equivalent to ω°, and ω stands for the angular frequency. Experimental rheology was carried out on a Mg(II)-metallohydrogel with a constant concentration of $Mg(NO_3)_2{\cdot}6H_2O$ ([Mg(II)] = 256 mg mL^{-1}). The results revealed a significantly higher storage modulus (G') in comparison to the loss modulus (G'') ($G' \gg G''$) (see Fig. 2a). This rheological data confirms the Mg(II)-metallohydrogel's retention of its gel-like structure and its display of solid-like behavior. Additionally, the Mg(II)-metallohydrogel showcases a notable tolerance limit, thanks to its considerably higher average storage modulus (G') compared to the loss modulus (G'') (see Fig. 2b). In Fig. 2b, a strain-sweep experiment was carried out on the Mg(II)-metallohydrogel material, maintaining a constant frequency of 6.27997 rad s^{-1}. The results revealed that the critical strain, causing the breakdown of the gel structure of the Mg(II)-metallohydrogel, occurred at a strain of 0.45%. This corresponded to the point where G' intersects with G'' (as shown in Fig. 2b).

However, it is worth noting that the storage modulus (G') exceeded the loss modulus (G'') until the strain reached approximately 0.1%, indicating a transition from gel to sol. To investigate the self-healing behavior, a thixotropy test was conducted (see Fig. 2c). Interestingly, the soft material remained in the gel state at a strain of about 0.01% but rapidly transformed into a sol state when the strain was abruptly increased to around 100%. Upon reducing the high strain, the soft material quickly reverted to a viscoelastic gel state. This cyclic process of transitioning from low to high strain

demonstrated the reversible transformation of the soft material from a gel to a sol state, affirming the self-healing behavior of the metallohydrogel.

Living organisms showcase remarkable instances of self-healing properties. The presence of electronegative N/O-atoms in the gelator 5-amino-1-pentanol suggests that the Mg@5AP metallohydrogel is a viable candidate for demonstrating self-healing properties. This is attributed to the gelator's propensity to form strong hydrogen bonds with solvent molecules and metal centers. The pure Mg@5AP metallohydrogel column, intended for testing its self-healing property, was prepared using the synthesis method outlined in Fig. 2d. This column was subsequently divided into three pieces, each measuring approximately 1–2 cm in length (Fig. 2d). Block pieces of Mg@5AP, some of which were doped with crystal violet and methyl red dyes, were reconnected by applying gentle pressure.

The pressed Mg@5AP blocks rapidly fused together, with a complete weld achieved in approximately 1 minute (Fig. 2e). The resulting solid structure displayed robust edges, capable of standing independently without requiring external support (Fig. 2e). The healed metallohydrogel displayed a robust interface that could withstand its own weight, as depicted in Fig. 2f. Consequently, the incorporation of different dyes did not compromise the strong self-healing characteristics of the Mg@5AP metallohydrogel, as evidenced in Fig. 2. Interestingly, the utilized dyes gradually dispersed throughout the entire gel structure, resulting in notable enhancements in diffusion properties at the interfaces of the cut blocks of the Mg@5AP metallohydrogel (see Fig. 2). Consequently, the monolith bridge formed by the Mg@5AP metallohydrogel exhibited excellent self-supporting qualities, as illustrated in Fig. 2g and h, and it could bear a remarkable load of approximately 100 grams. Furthermore, the stability of these monoliths, even when subjected to the force of gravity, is evident in Fig. 2i. Additionally, to explore the moldability of the Mg@5AP metallohydrogel, it was fashioned into the shapes of a heart, retaining its structural integrity and self-healing property without any fluid loss and without needing external support. This demonstrates its exceptional moldable characteristics (Fig. 2j). Moreover, Fig. 2k illustrates a sketch illustrating the application of Mg@5AP metallohydrogel as an ink. The hydrogel was also employed to create nodule-shaped patterns using a surgical syringe, highlighting its suitability for injection purposes (Fig. 2l).

The self-assembly mechanism of the Mg@5AP metallohydrogel formed from magnesium nitrate and 5-amino-1-pentanol (5AP) in water involves a synergistic interplay of coordination bonding, hydrogen bonding, and hydrophobic interactions. Magnesium nitrate dissociates in water to release Mg^{2+} ions, which act as coordination centers. The gelator, 5AP, contains both an amine ($-NH_2$) and a hydroxyl (–OH) functional group, enabling it to serve as a versatile ligand. The Mg^{2+} ions coordinate with the amine and hydroxyl groups of 5AP, creating a cross-linked network. Simultaneously, hydrogen bonding between adjacent 5AP molecules and the nitrate ions further stabilizes the network structure. The hydrophobic alkyl chain of 5AP contributes to the self-assembly by promoting aggregation *via* hydrophobic interactions, driving the gelation process.

Magnesium was chosen due to its biocompatibility, abundance, and ability to form stable coordination complexes, while 5AP was selected as the organic component for its dual functional groups – an amine and a hydroxyl – which enable robust hydrogen bonding and coordination with magnesium. This combination promotes gelation under mild conditions and ensures the stability of the metallohydrogel.

3.2. Microstructural study

The FESEM microstructural analysis of Mg@5AP metallohydrogel reveals a distinctive hierarchical network characterized by mixed flake and rod-like patterns (as depicted in Fig. S1a and b, ESI†). These structural arrangements within the Mg@5AP metallohydrogel emerged through the synergistic combination of magnesium nitrate hexahydrate and 5-amino-1-pentanol molecules, facilitated by direct mixing. The resulting FESEM image showcases the interconnected mixed flake and rod-like morphology, underscoring the intricate nature of the formed networks.

The microstructure of the materials and variations in their crystal structure are investigated using transmission electron microscopy (TEM). In Fig. 3a, the mixed flake and rod-shaped structural morphology of the Mg@5AP metallohydrogel is evident through low-magnification high angle annular dark field (HAADF) bright field STEM imaging. Interplanar distances can be precisely measured from TEM analysis and may be found to be around 0.249 nm, 0.246 nm, 0.253 nm, 0.230 nm, and 0.207 nm in different places where crystallinity is shown (Fig. 3b). This provides us with a better understanding of the crystalline structure and overall stability of the material. From the HRTEM image, it has been revealed that this Mg-based metallogel is polycrystalline. This information is crucial for the application in catalysis, energy storage, and magnetic devices. The TEM investigation effectively explains the nanoscale properties of the metallohydrogels which opens up new opportunities for research in materials science and advancement in nanotechnology. Furthermore, TEM images of Mg@5AP metallohydrogel can be used to measure the size of the particles and the interplanar distance inside the structure of the material accurately.

From TEM images, we are able to identify the size distribution of the Mg particles, which offers crucial information on their shape and homogeneity. The average size of Mg particles is 42.56 nm, according to the histogram plot shown in Fig. 3c, and their average area is 39.01 nm^2 (Fig. 3d). The presence of essential elements, including C, O, N, and Mg, derived from magnesium nitrate hexahydrate and 5-amino-1-pentanol molecules, crucial for the formation of the Mg@5AP metallohydrogel networks, is confirmed through elemental composition mapping by EDX (Fig. 3e–i).

3.3. FT-IR analysis of the Mg@5AP metallohydrogel

The FT-IR spectral analysis of the Mg@5AP metallohydrogel in its xerogel state provides insights into the primary interactions between 5-amino-1-pentanol and the source of Mg(II) in the metallohydrogel formation (Fig. S2, ESI†). Within the spectrum, wide and broad peaks within the range of 3380–3240 cm^{-1}

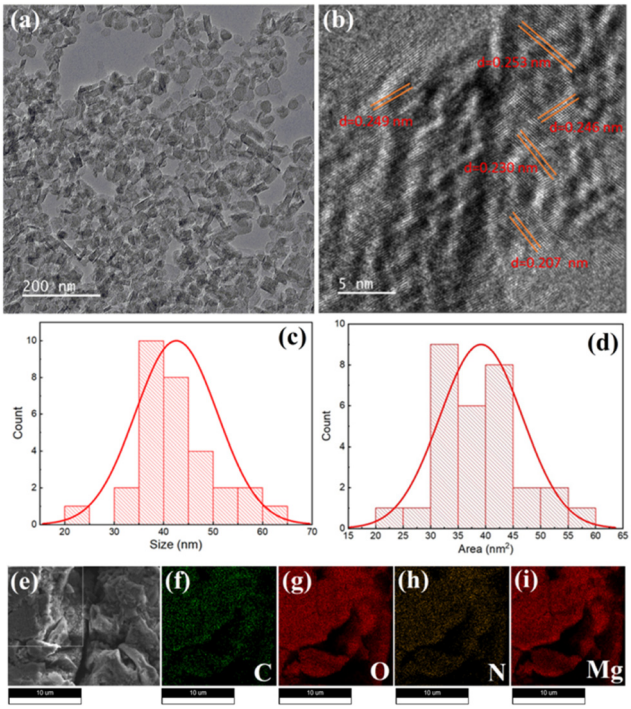

Fig. 3 (a) Transmission electron microscopy (TEM) image of the Mg@5AP metallohydrogel showing mixed flake and rod-shaped structural morphology (scale bar: 500 nm). (b) High-resolution TEM (HRTEM) image revealing the polycrystalline nature of the Mg@5AP metallohydrogel with interplanar distances of approximately 0.249 nm, 0.246 nm, 0.253 nm, 0.230 nm, and 0.207 nm at different regions (scale bar: 2 nm). (c) Histogram plot illustrating the particle size distribution with an average size of 42.56 nm. (d) Histogram plot representing the particle area distribution with an average area of 39.01 nm^2. (e)–(i) Energy dispersive X-ray (EDX) elemental mapping showing the spatial distribution of carbon (C), oxygen (O), nitrogen (N), and magnesium (Mg) within the Mg@5AP metallohydrogel (scale bars: 1 μm).

correspond to O–H stretching vibrations, while vibrational modes at 2950 cm^{-1} and 2086 cm^{-1} are attributed to C–H stretching vibrations and C–H bending vibrations respectively. Additionally, the vibrational modes associated with the peaks at 1640 cm^{-1} and 1355 cm^{-1} correspond to N–O stretching and C–N stretching, respectively. Furthermore, to underscore the robustness of the association between 5-amino-1-pentanol and the aqueous solution of magnesium nitrate, an observable peak at 640 cm^{-1} can be identified in the spectrum (Fig. S2, ESI†). This specific peak signifies the presence of Mg–O bonds, providing further confirmation of the metallohydrogelation process.

3.4. Optical characterization

To establish the optical properties of the synthesised Mg@5AP based metallohydrogel, the UV-vis absorption spectra were analysed using the Tauc's Plot, as shown in Fig. S3 (ESI†). A wavelength range of 250 nm to 800 nm was used for the optical measurement (see the UV-vis absorption spectra). Using the UV-vis spectrum, we used Tauc's equation (eqn (1)) to calculate the optical bandgap (E_g) of the Mg@5AP metallohydrogel:

$$(\alpha h\nu)^n = A(h\nu - E_g) \quad (1)$$

where α, E_g, h, and ν are the absorption coefficient, band gap, Planck's constant and frequency of the light respectively. In the processes of electron transitions, the exponent "n" is a constant. "A" is also constant and it has a value of 1. Using $n = 2$, the direct optical band gap was computed. We determined the direct optical band gap (E_g), which is assumed to be 4.90 eV, by extending the linear region of the plot $(\alpha h\nu)^2$ *vs.* $h\nu$ (Fig. S3, ESI†) to the region where absorption vanishes.

3.5. Device fabrication

We created a device with a lateral Schottky diode-like structure based on a metal–semiconductor junction in the ITO (Indium Tin Oxide)/Mg@5AP/ITO configuration (Device 1) to conduct the electrical characterization of the synthesised material in this study. We used the Doctor's blade method to create a thin coating of synthesised Mg@5AP metallohydrogel on an ITO-coated glass substrate to make the junction device. The film was annealed to remove the solvent. ITO is the perfect material for research involving photo-excitations because it is both an excellent conductor and an optically transparent substance in the visible region.

We prepared two sandwiched-like structures of ITO/Mg@5AP/Cu (referred to as Device 2) and Cu/Mg@5AP/Cu (referred to as Device 3) to make RRAM (Resistive Random Access Memory) devices based on the Mg@5AP metallohydrogel. In both configurations, the bottom electrodes were cleaned using an ultrasonicator. Then the Mg@5AP metallohydrogel was deposited onto the substrate. After that the top electrode was placed on the sample for making this device.

The device structures are given in Table 1.

3.6. Electrical characterization of devices

In order to provide accurate measurements of the material's semiconductor nature, the charge transport characteristics of the Mg@5AP metallohydrogel in the thin film geometry were measured in a two-probe setup. There is no visible conduction in the voltage range (−5 V to +5 V), where the *I–V* curve of device 1 is shown in Fig. S4 (ESI†) on a linear scale. In both positive and negative polarity, it was observed that the current quickly increased with voltage beyond this region. After measuring the *I–V* characteristics, the primary diode characteristics were derived from the non-linear Schottky diode's *I–V* curve using the thermionic emission theory (TE Theory). To investigate the conduction behaviour of such systems, Cheung proposed this technique. The following equations have been used to evaluate the measured *I–V* curve:

$$I = I_0 \exp\left(\frac{qV}{\eta k_B T}\right)\left[1 - \exp\left(\frac{-qV}{\eta k_B T}\right)\right] \quad (2)$$

Table 1 Different devices with their structure

Device name	Device structure
Device 1	ITO/Mg@5AP/ITO
Device 2	ITO/Mg@5AP/Cu
Device 3	Cu/Mg@5AP/Cu

$$I_0 = AA^*T^2 \exp\left(\frac{-q\phi_B}{k_B T}\right) \quad (3)$$

Here, I_0 = saturation current, q = electronic charge, k_B = Boltzmann's constant, T = temperature, V = applied voltage, A = effective diode area, η = ideality factor, Φ_B = barrier potential height, R_S = series resistance, and A^* = effective Richardson constant which is considered to be 32 A K^{-2} cm^{-2} for this device.

We also plotted the log I *vs.* log V graph, which is shown in Fig. S4 (ESI†) (right: inset) to understand the conduction mechanism. In the lower voltage zone, the current followed ohmic conduction behaviour with the slope of m = 1.10, and in the higher voltage region, it followed the Space charge limited conduction mechanism with a slope of m = 4.39.

$$\frac{dV}{d(\ln I)} = \left(\frac{\eta k_B T}{q}\right) + IR_S \quad (4)$$

$$H(I) = V - \left(\frac{\eta k_B T}{q}\right) \ln\left(\frac{I}{AA^*T^2}\right) \quad (5)$$

$$H(I) = IR_S + \eta\phi_B \quad (6)$$

The series resistance, ideality factor and barrier potential height were determined using eqn (4)–(6). Cheung suggested these equations. We plotted the graphs of $dV/d(\ln I)$ *vs.* I and H *vs.* I to obtain the diode parameters of device 1, as shown in Fig. S5 (ESI†). The intercept of the H *vs.* I graph was used to determine the barrier height, and the intercept of the $dV/d(\ln I)$ *vs.* I graph was used to obtain the ideality factor (η). We determined the ideality factor (η) which is 13.497. This value is higher than the ideal value of 1.1. The divergence of these results could be caused by the presence of interface states, series resistance at the interface, and the presence of inhomogeneities in the Schottky barrier itself.

A barrier height (ϕ_B) of 0.0258 eV was established for device 1. A lower barrier potential height and a higher ideality factor are crucial for fabricating a Schottky diode, as they directly influence its performance and efficiency in the prepared diode structure. We calculated the slope of the $dV/d(\ln I)$ *vs.* I graph as well as the H *vs.* I graph to obtain the value of the series resistance, which is 1358.04 Ω. It may be concluded that such diode layouts can be useful for semiconductor electronics design by taking into account all the measured features.

From the IV measurements, it is also possible to analyse the resistive switching behaviour of the Mg@5AP metallohydrogel-based heterostructure (Fig. 4 (right: inset)), where ITO acts as the bottom electrode and Cu acts as the top electrode in device 2.

To prevent any leakage contribution to the I–V measurements, the compliance current (CC) is set at 100 mA before starting any measurements of our studies. The I–V trajectory of device 2 is shown on a linear scale in Fig. 4. In this instance, the I–V measurements are performed as follows: 0 V → 10 V → −10 V → 10 V. The sequence of the applied voltage is shown by the arrows. The IV characteristics show a complete hysteresis, which is a signature of memristor behaviour. From point 1 to point 2, the current across the low-voltage region increases linearly. When the applied voltage increases, the current–voltage graph demonstrates a nonlinear nature above a certain voltage of 5.85 V at point 2 and then the current increases rapidly. Then the device is switched from a higher resistance state (HRS) to a lower resistance state (LRS), as indicated by the SET voltage (V_{SET} = 10 V). From point 3 to point 4, the current increases while the device remains in the ON state. When the voltage drops from point 4 to point 5, the device enters into an OFF state and the current starts to decay quickly. After a reverse cycle, the current will increase until it reaches an LRS at point 5. When the RESET value (V_{RESET}) reaches −9.98 V, the device returns to the HRS mode. The transfer from LRS to HRS is defined by the RESET method, which is indicated by the arrow between points 5 and 6. This is a crucial indicator of the bipolar resistive switching behaviour of this device because a negative voltage is required to return the device to its previous resistance state. The I–V characteristic of the device 2 is displayed on a semi-logarithmic scale in Fig. 4 (inset (left)). The main reason for increasing and decreasing in current is the formation and rupture of conductive filament-type structures, which tries to switch the device between the ON and OFF state. This mechanism is explained in the later part.

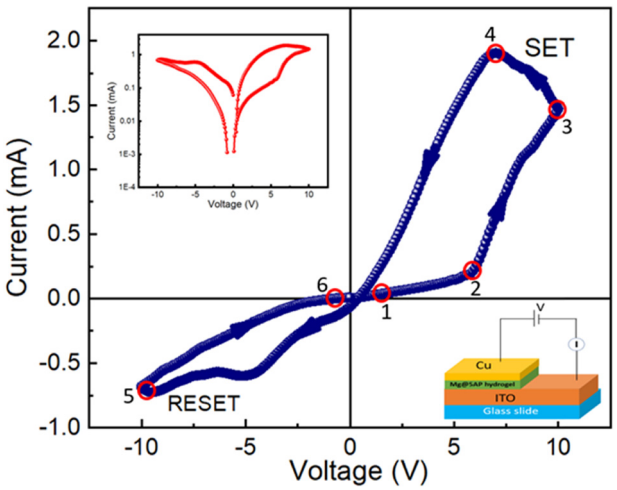

Fig. 4 Schematic representation of a glass/ITO/Mg@5AP/Cu-based device (right: inset), along with I–V characteristics plotted on a linear scale for the same device (Points 1 to 2 indicate a linear increase in current, Points 2 to 3 indicate a rapid increase in current, Points 3 to 4 also indicate an increase in current, Points 4 to 5 indicate an abrupt decrease in current up to −10 V, Points 5 to 6 indicate a change in direction of current and then current increases continuously up to 0 V) and I–V curve of the glass/ITO/Mg@5AP/Cu based device in semi-logarithmic scale (left: inset).

To understand the conduction mechanism and the charge transport mechanism of device 2, we have also plotted the I–V curve in a logarithmic scale throughout the SET procedure (shown in Fig. S6, ESI†). Here, it is observed that the current changes linearly from 0 to 3 V with a slope of m = 1.14. This current follows Ohmic conduction behaviour. From 3 V to 5 V, it also follows Ohmic conduction behaviour with the slope of

m = 1.38 and in the higher voltage region from 5 V to 10 V, it obeys a space charge conduction mechanism with a slope of m = 5.69. It is confirmed that the space charge limited conduction behaviour occurs when the slope is greater than 2.

In order to measure the resistive switching characteristics of device 3, Cu acts as the top and bottom electrodes. In Fig. 5, the I–V curve shows the behaviour of a memristor during full voltage cycling with discrete LRS and HRS states in the presence of SET and RESET operations (V_{SET} = 7.17 V and V_{RESET} = −9.98 V). This resistive switching behaviour of device 3 is comparable with device 2. The I–V characteristic of device 3 on a semi-logarithmic scale is shown in Fig. 5 (inset (left)).

To understand the conduction mechanism and the charge transport process for device 3, we have also fitted the I–V curve in a logarithmic scale during the SET process (Fig. S7, ESI†). In the lower voltage range of 0 V to 2 V, the current is seen to vary linearly with a slope of m = 1.06 and from 2 V to 5 V, the slope of m = 1.19 that means it shows Ohmic conduction behaviour. But in the higher voltage range of 5 V to 10 V, it follows a space charge limited conduction mechanism with a slope of m = 5.10.

To understand the consistency of the switching process, we have also measured the endurance test for 5000 cycles at room temperature, as shown in Fig. S8 (ESI†). The switching process of this device 3 is reliable up to 5000 switching cycles. The average ON/OFF ratio of this device, which we have calculated from the endurance test to be around 120, shows highly robust switching behaviour. This indicates that there won't be any degradation in the device's memory response, which is advantageous for practical application in less expensive memory circuit design. A comparison of I_{ON}/I_{OFF} observed in other oxide materials at room temperature (shown in Table 2).

Numerous mechanisms, such as the formation of the Schottky barrier with electrochemical migration, redox reactions, and valence change memory can be used to explain the physical causes of the resistive switching process. According to our research, the processes of valence change memory (VCM) and electrochemical metallization (ECM) are influenced by the mobility of oxygen defects and metal cations. Here, it is shown that both metal ions and oxygen vacancies have a considerable impact on the change in resistance (Fig. 6). In the semiconducting layers of device 2, conducting filaments are formed and the main reason behind this filament formation is the movement of Cu ions, Mg ions, and oxygen vacancies. It is possible to explain the change from the HRS to LRS in the semiconducting layers by the formation and rupturing of the Cu filaments. This work demonstrates that the resistive switching behaviour of device 2 is mostly caused by the movement of Cu ions and oxygen vacancies. As we already know that their chemical formula is $Cu \rightarrow Cu^{2+} + e^{-}$, Cu ions may move in the direction of an applied electric field and ionize in the presence of an electric field. When we apply a positive voltage, Cu^{2+} ions, Mg ions, and oxygen vacancies travel towards the intermediate layer, where they transform into metallic Cu. The device changes from HRS to LRS after the SET process is complete and then the conductivity of this layer will increase and the concentration of Cu ions, Mg ions, and oxygen vacancies will go to the bottom electrode. Until a sufficient voltage with the opposite polarity is applied to electrochemically dissolve the Cu filaments and oxygen vacancies for the RESET operation, the device remains in the LRS state. The device enters the HRS when negative voltage is provided and its conductivity will decrease at the same time. At the end of the procedure Cu^{2+},

Table 2 Comparison of SET and RESET values with different oxide materials

System	Type	V_{SET}	V_{RESET}	I_{ON}/I_{OFF}	Ref.
$La_{0.7}Sr_{0.3}MnO_3$-rGO	Bulk	9.5	−9.7	10	45
$LaCoO_3$-graphene	Bulk	9.8	−8.1	40	46
Cu/Mg@5AP/Cu	Thin Film	7.17	−9.98	120	Current work

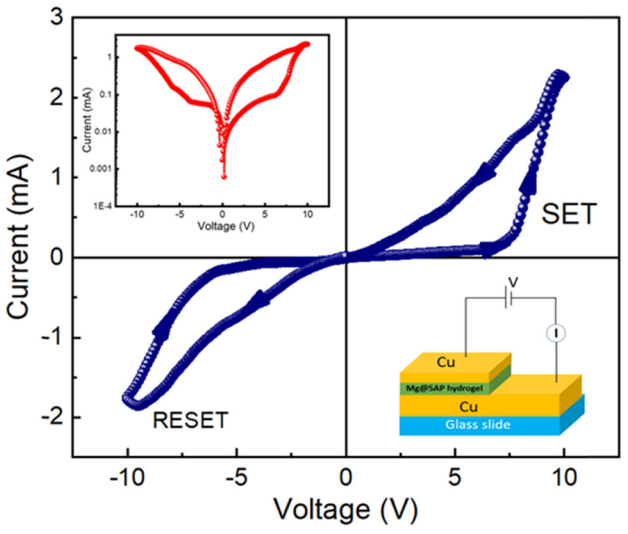

Fig. 5 Schematic representation of a glass/Cu/Mg@5AP/Cu-based device (right: inset), along with I–V characteristics plotted on a linear scale for the same device and the I–V curve of the glass/Cu/Mg@5AP/Cu based device in semi-logarithemic scale (left: inset).

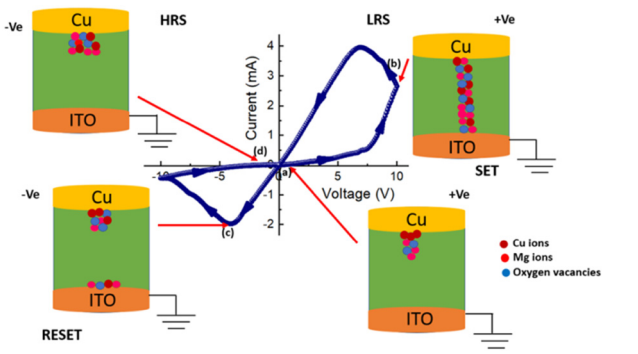

Fig. 6 This diagram illustrates the resistive switching process of a glass/ITO/Mg@5AP/Cu-based device using the conductive filament model. The following places have been located using the I–V curve: (a) The ions move towards the intermediate layer after applying a positive voltage of 0.5 V; (b) at 9.94 V, the Cu ions, Mg ions, and oxygen vacancies produced a conducting filament-type structure; (c) at −4 V, the Cu ions, Mg ions, and oxygen vacancies return to the top electrode; and (d) at −0.5 V, all of the ions are gathered at the top electrode and switched into HRS.

Mg ions, and oxygen vacancies return to the top electrode. In this method, the resistive switching behaviour of device 3 can be explained by the migration of Cu^{2+} ions, Mg ions, and oxygen vacancies.

3.7. Antibacterial activity of the Mg@PEH gel

The antibacterial activity of the Mg@5AP gel was initially evaluated by observing the size of the inhibition zones surrounding the gel when added against the KP and MRSA grown spread plates separately. Notably, the gel showed a well-defined inhibition zone measuring 1.3 cm in width, against both the Gram-negative and Gram-positive strains, whereas in CX-30 no zone of inhibition observed, suggesting the broad-spectrum bactericidal property of the gel (Fig. 7a and b).

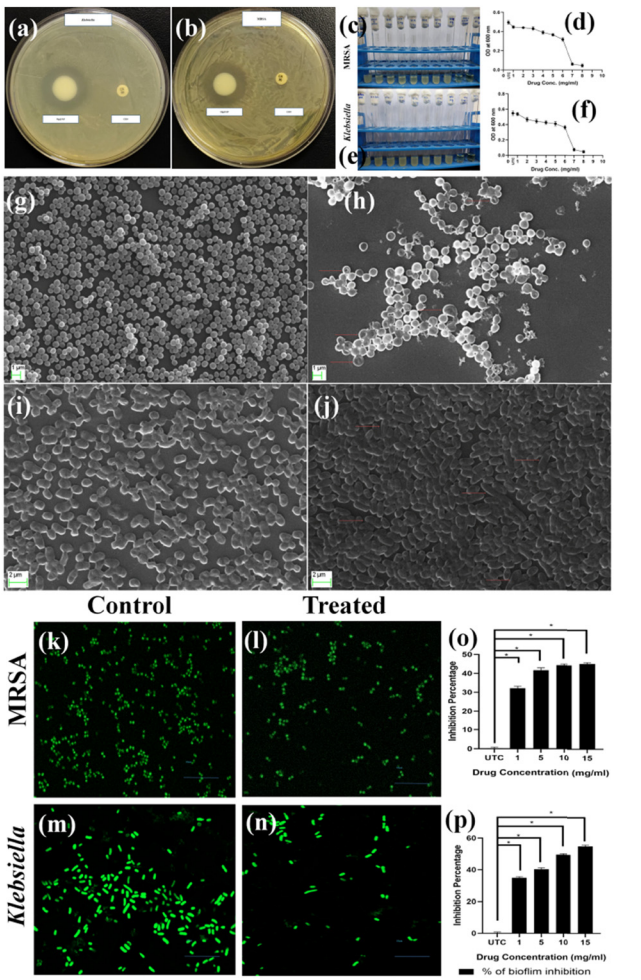

Fig. 7 Antibacterial assay of Mg@5AP against (a) *Klebsiella* and (b) MRSA showing the zone of inhibition. Minimum inhibitory concentration (MIC) of Mg@5AP on the growth of MRSA (c) and (d) and KP (e) and (f). SEM images of MRSA (g) control, (h) treated with Mg@5AP & KP, (i) control, and (j) treated with Mg@5AP metallohydrogel. Confocal laser scanning microscopic images show the effect of Mg@5AP on the biofilm of MRSA (k) control, (l) treated with Mg@5AP & KP, (m) control, and (n) treated with Mg@5AP. Quantification of the biofilm inhibition by Mg@5AP against (o) MRSA & (p) KP.

3.8. Minimum inhibitory concentration (MIC)

The standard broth micro-dilution technique was used to determine the MIC of Mg@5AP against KP and MRSA. The Mg@5AP metallohydrogel exhibited significant antibacterial effects against both the strains, with a concentration range of 1 to 8 mg mL^{-1}. Based on optical density of both the treated bacterial strains, the Minimum Inhibitory Concentration (MIC) was determined to be within the range of 6 to 7 mg mL^{-1}, when compared with the untreated control. Consequently, sub-MIC doses were used for subsequent biological studies (Fig. 7c–f).

3.9. Scanning electron microscopy (SEM)

The SEM photographs for both MRSA and KP shown that the untreated groups (Fig. 7g and i) displayed bacteria with consistent shapes, densely arranged cells, and maintained uniformity in morphology. On the other hand, significant structural alterations were found following 24-hour exposure to Mg@5AP, both in MRSA and KP (Fig. 7h and j). For KP, the cells were elongated, and some changes in cell morphology were seen (Fig. 7j), whereas increased cell size, porous cell membrane, and disruption in cell morphology were found in MRSA (Fig. 7h). Results suggested that Mg@5AP had an impact on bacterial morphology, suggesting its potential as an agent for inducing significant inhibitory effects on both *Klebsiella* and MRSA.

3.10. Biofilm inhibition assay

The crystal violet (CV) assay was used to determine the effectiveness of different doses of Mg@5AP, diluted in 1% DMSO, against the developed mature biofilms. The CV assay demonstrated a significant effect on bacterial biofilm, when treated with Mg@5AP. At a concentration of 15, 10, 5, and 1 mg mL^{-1}, the biofilm in KP was reduced by up to 54.23%, 48.90%, 39.01%, and 35.71%, respectively. Similar results were obtained for MRSA also, where the biofilm was reduced by 44.57%, 44.40%, 41.57%, and 31.21% respectively, when treated with the same corresponding concentration of Mg@5AP (Fig. 7p and o).

3.11. Confocal microscopy

The effectiveness of the anti-biofilm activity of Mg@5AP diluted in 1% DMSO was further validated through confocal laser scanning microscopy. The images of MRSA and KP biofilms treated with sub-MIC concentrations of Mg@5AP also proved altered morphology compared with the untreated control. The untreated control of MRSA & KP displayed (Fig. 7k and m) a higher presence of microorganisms than the treated group (Fig. 7l and n). The application of acridine orange resulted in the manifestation of green fluorescence, affirming a decrease in organism population in both MRSA and KP.

3.12. *In vivo* Mg@5AP metallohydrogel mediated wound healing assay

We continued the investigations using an *in vivo* wound healing assay to confirm the antibacterial activity and explore the topical therapeutic potential of Mg@5AP. All of the mice in the groups were injured on day 0 (the wound day), and groups 2

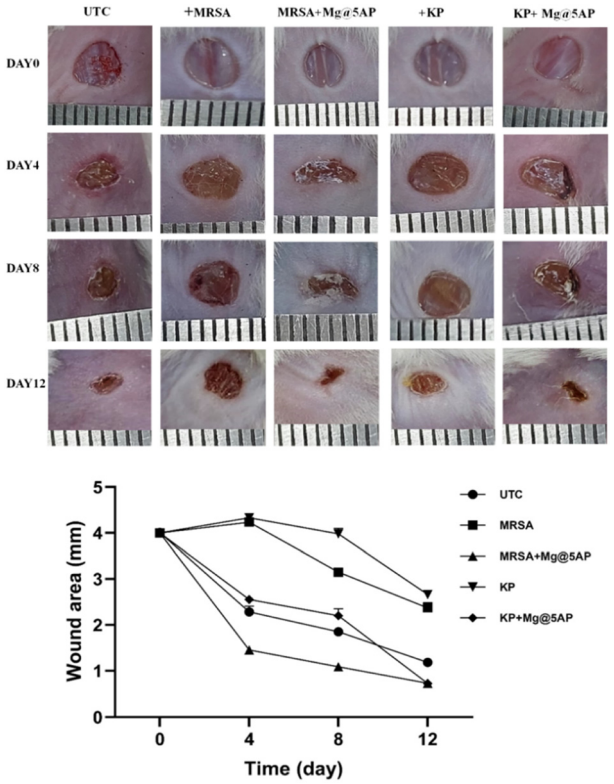

Fig. 8 Digital photographs (with scale bar) of the wound healing property of Mg@5AP on KP and MRSA infected wounds at different days along with infected wounds without treatment as the positive control and only wound as the negative control where no infection and treatment were administered.

and 3 were subsequently infected with Gram-negative Klebsiella (KP) and Gram-positive MRSA, respectively. For group 4 and 5, following infection with KP and MRSA separately, the wounded mice were further treated with Mg@5AP gel, as a topical agent on every alternate day on the wound area. After twelve days of treatment, the infected wounds (group 4 & 5) were healed significantly compared to the wounds without treatment.

Compared to the other groups, group 2 & 3 mice have bigger wound areas, suggesting that KP and MRSA may interact with the wound to impede healing. The results from Fig. 7k–n confirm that the Mg@5AP gel had excellent wound healing potentiality, and can also be applied as a topical agent against bacterial infection (Fig. 8).

3.13. HE staining

In the untreated control sample, the epidermal layer exhibited normal nuclear morphology, along with the presence of well-defined hair shafts. Additionally, the dermal tissue displayed appropriate organization and structure. In the *Klebsiella*-infected group, an uneven epidermal layer was observed, along with the infiltration of the dermal tissue characterized by disorganized nuclei. Moreover, a reduction was noted in the number of hair follicles. The MRSA-infected group exhibited considerable disorganization of the epidermal layer, accompanied by

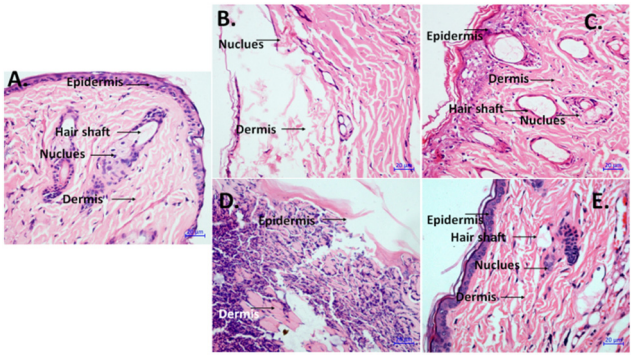

Fig. 9 HE staining of the control and Mg@5AP treated group on wound regeneration processes on the 8th day. (A) UTC group, (B) *Klebsiella* infected group, (C) MRSA infected group, (D) Mg@5AP treated *Klebsiella* infected group, and (E) Mg@5AP treated MRSA infected group.

degenerated and shrunken nuclei. Although hair shafts were present, they exhibited an abnormal appearance (Fig. 9).

Upon treatment with Mg@5AP, the *Klebsiella*-infected group evidenced a remarkable improvement in the epidermis as compared to the control and infected groups. The nuclear structure showed signs of reversal, and the hair shafts appeared nearly normal. The administration of Mg@5AP in the MRSA-infected group effectuated a striking alleviation of prior symptoms in the epidermis, which displayed a normal cellular arrangement and enhanced nuclear morphology as compared to the control and infected groups. A notable increase was recorded in the number of hair shafts, and improved structural integrity was evident. Additionally, the dermal layer exhibited a continuous organization of cells (Fig. 8).

3.14. Haemolysis assay

Hemolysis was conducted to evaluate the biocompatibility of Mg@5AP and assesses the damage to red blood cells (RBCs) qualitatively. After centrifugation the positive control shows a red color that signifies release of hemoglobin into the buffer from RBCs, whereas all the other samples show a clear color in the soup and precipitation of RBCs in the pellet that suggest no damage to RBCs. The Mg@5AP compound showed no haemolytic potential at the tested concentration (Fig. S9, ESI†) (*i.e.* half MIC, MIC and double MIC).

3.15. Cytotoxicity assay [MTT assay]

Cell viability was evaluated using the MTT assay. Compared to the control group, HEK293T cells treated with increasing concentrations of Mg@5AP showed no significant reduction in viability. Even at the highest concentration *i.e.* 12 mg mL^{-1}, cell viability remained above 80% (Fig. S10, ESI†). Based on these findings, we may conclude that Mg@5AP exhibits low toxicity toward HEK293T (a non-cancerous cell line).

4. Conclusions

In summary, a novel Mg(II)-metallohydrogel was efficiently synthesized by rapidly mixing magnesium nitrate hexahydrate

with 5-amino-1-pentanol in an aqueous solution at room temperature. The formation of this self-assembled Mg(II)-metallohydrogel network can be attributed to the coordinated and cooperative interactions between the metal ions and the ligand 5-amino-1-pentanol in water. To evaluate its mechanical stability, rheological analysis and thixotropic data were utilized. Microstructural examinations using FESEM and TEM revealed the hierarchical mixed flake rod-like architecture of the Mg(II)-metallohydrogel, while FT-IR spectroscopy characterized intermolecular interactions. Optical band-gap measurements indicated the semiconducting nature of this metallohydrogel. Furthermore, a metal–semiconductor junction-based device was fabricated and this device exhibited Schottky diode characteristics. Additionally, two types of resistive random access memory (RRAM) devices, ITO/Mg@5AP/Cu and Cu/Mg@5AP/Cu, were fabricated, both displaying bipolar resistive switching behavior in their *I–V* characteristics. This behavior was attributed to the formation and rupture of conduction filaments between the vertical electrodes. Impressively, these devices demonstrated non-volatile and non-destructive switching properties with an excellent ON/OFF ratio of approximately 120 over 5000 switching cycles. Recent research suggests that the Mg(II)-metallohydrogel is a promising candidate for non-volatile memory applications due to its robust resistive switching behavior, high endurance, and substantial ON/OFF ratio. Additionally, its stable switching performance and versatile functionalities make it an appealing option for applications in neuromorphic computing, neural circuit design, and the development of flexible electronic devices using thin films of Mg@5AP metallohydrogel for advanced technological purposes. This gel showed biocompatibility in the haemolysis assay and demonstrated no cytotoxicity when the HEK 293T cells were treated with this compound. However, the Mg@5AP gel attributed broad-spectrum antibacterial properties when drug resistants *Klebsiella* and *Staphylococcus* were treated separately. On application of Mg@5AP, a notable improvement in the epidermis, dermis, hair shaft, and nuclear structure was demonstrated during wound regeneration phases when compared to the MRSA- and *Klebsiella*-infected groups. Based on these findings, we may conclude that Mg@5AP exhibits significant wound healing efficacy when performing a wound healing assay using BALB/c mice as the model. Moreover, the Mg@5AP metallohydrogel demonstrates antibacterial, antibiofilm, antisepsis, and wound healing properties, underscoring its potential as a topical therapeutic agent. This study effectively explores the multifaceted applications of Mg(II)-ion-based metallohydrogels, offering valuable insights to readers in the field of materials science.

Data availability

The authors declare that the data supporting the findings of this study are available within the paper and its ESI.† Should any raw data files be needed in another format they are available from the corresponding author upon reasonable request.

Conflicts of interest

The authors declare no competing financial interests.

Acknowledgements

S. D. expresses gratitude to the UGC, New Delhi, for the conferred Dr DS Kothari Postdoctoral Fellowship (Award letter number: No. F.4-2/2006 (BSR)/CH/19-20/0224). S. B. appreciates the support from a DST Inspire Faculty Research Grant (Faculty Registration No.: IFA18-CH304; DST/INSPIRE/04/2018/000329).

Notes and references

1 N. M. Sangeethaa and U. Maitra, Supramolecular gels: Functions and uses, *Chem. Soc. Rev.*, 2005, **34**, 821–836.
2 P. Dastidar, Supramolecular gelling agents: can they be designed?, *Chem. Soc. Rev.*, 2008, **37**, 2699–2715.
3 M. D. Ward, Photo-induced electron and energy transfer in non-covalently bonded supramolecular assemblies, *Chem. Soc. Rev.*, 1997, **26**, 365–375.
4 R. Madueno, M. T. Räisänen, C. Silien and M. Buck, Functionalizing hydrogen-bonded surface networks with self-assembled monolayers, *Nature*, 2008, **454**, 618–621.
5 I. W. Hamley, Nanotechnology with Soft Materials, *Angew. Chem., Int. Ed.*, 2003, **42**, 1692–1712.
6 T. Kato, N. Mizoshita and K. Kishimoto, Functional Liquid-Crystalline Assemblies: Self-Organized Soft Materials, *Angew. Chem., Int. Ed.*, 2006, **45**, 38–68.
7 P. Terech and R. G. Weiss, *Chem. Rev.*, 1997, **97**, 3133; Low Molecular Mass Gelators: Design, Self-Assembly, Function, ed. F. Fages, *Topics in Current Chemistry*, SpringerVerlag, Berlin, 2005, p. 256.
8 J. D. D. de Jong and B. L. Feringa, *Molecular gels, materials with self-assembled fibrillar networks*, Springer, The Netherlands, 2006.
9 J. Puigmartí-Luis, V. Laukhin, Á. Pérez del Pino, J. Vidal-Gancedo, C. Rovira, E. Laukhina and D. B. Amabilino, Supramolecular conducting nanowires from organogels, *Angew. Chem., Int. Ed.*, 2007, **46**, 238.
10 Z. Yang, P.-L. Ho, G. Liang, K.-H. Chow, Q. Wang, Y. Cao, Z. Guo and B. Xu, Using β-lactamase to trigger supramolecular hydrogelation, *J. Am. Chem. Soc.*, 2007, **129**, 266.
11 S. Dhibar, A. Dey, A. Dey, S. Majumdar, D. Ghosh, P. P. Ray and B. Dey, Development of Supramolecular Semiconducting Mn(II)-Metallohydrogel Based Active Device with Substantial Carrier Diffusion Length, *ACS Appl. Electron. Mater.*, 2019, **1**, 1899–1908.
12 J. W. Steed and J. L. Atwood, *Supramol. Chem.*, 2009, **14**, 888–893.
13 J. W. Steed, Supramolecular gel chemistry: developments over the last decade, *Chem. Commun.*, 2011, **47**, 1379–1383.
14 F. Fages, F. Vögtle and M. Žinic, Cholesterol-based gelators, *Top. Curr. Chem.*, 2005, **256**, 77–131.

15 M. George, G. Tan, V. T. John and R. G. Weiss, Urea and thiourea derivatives as low molecular-mass organogelators, *Chem. - Eur. J.*, 2005, **11**, 3243–3254.
16 S. J. Wezenberg, C. M. Croisetu, M. C. A. Stuart and B. L. Feringa, Reversible gel-sol photoswitching with an overcrowded alkene-based bis-urea supergelator, *Chem. Sci.*, 2016, **7**, 4341–4346.
17 E. R. Draper and D. J. Adams, Photoresponsive gelators, *Chem. Commun.*, 2016, **52**, 8196–8206.
18 J. Yan, J. Liu, P. Jing, C. Xu, J. Wu, D. Gao and Y. Fang, Cholesterol-based low-molecular mass gelators towards smart ionogels, *Soft Matter*, 2012, **8**, 11697–11703.
19 F. Fages, F. Vögtle and M. Žinic, Systematic design of amide- and urea-type gelators with tailored properties, *Top. Curr. Chem.*, 2005, **256**, 77–131.
20 C.-C. Tsou and S.-S. Sun, New Fluorescent Amide-Functionalized Phenylethynylthiophene Low Molecular Weight Gelator, *Org. Lett.*, 2006, **8**, 387–390.
21 X. Du, J. Zhou, J. Shi and B. Xu, Supramolecular Hydrogelators and Hydrogels: From Soft Matter to Molecular Biomaterials, *Chem. Rev.*, 2015, **115**, 13165–13307.
22 C. Narayana, R. K. Upadhyay, R. Chaturvedi and R. Sagar, A versatile carbohydrate based gelator for oil water separation, nanoparticle synthesis and dye removal, *New J. Chem.*, 2017, **41**, 2261–2267.
23 J. H. Jung, G. John, M. Masuda, K. Yoshida, S. Shinkai and T. Shimizu, Self-assembly of a sugar-based gelator in water: Its remarkable diversity in gelation ability and aggregate structure, *Langmuir*, 2001, **17**, 7229–7232.
24 C. Tomasini and N. Castellucci, Peptides and peptidomimetics that behave as low molecular weight gelators, *Chem. Soc. Rev.*, 2013, **42**, 156–172.
25 S. Samai, J. Dey and K. Biradha, Amino acid based low-molecular-weight tris(bis-amido) organogelators, *Soft Matter*, 2011, **7**, 2121–2126.
26 S. Dhibar, A. Dey, A. Dey, S. Majumdar, A. Mandal, P. P. Ray and B. Dey, The development of a rapid self-healing semiconducting monoethanolamine-based $Mg(OH)_2$ metallogel for a Schottky diode application with a high ON/OFF ratio, *New J. Chem.*, 2019, **43**, 15691–15699.
27 B. Jiang, L.-J. Chen, G.-Q. Yin, Y.-X. Wang, W. Zheng, L. Xu and H.-B. Yang, Multiphase transition of supramolecular metallogels triggered by temperature, *Chem. Commun.*, 2017, **53**, 172–175.
28 C. K. Karan and M. Bhattacharjee, Self-Healing and Moldable Metallogels as the Recyclable Materials for Selective Dye Adsorption and Separation, *ACS Appl. Mater. Interfaces*, 2016, **8**, 5526–5535.
29 Z. Yao, Z. Wang, Y. Yu, C. Zeng and K. Cao, Facile synthesis and properties of the chemo-reversible and highly tunable metallogels based on polydicyclopentadiene, *Polymer*, 2017, **119**, 98–106.
30 C. A. Offiler, C. D. Jones and J. W. Steed, Metal 'turn-off', anion 'turn-on' gelation cascade in pyridinylmethyl ureas, *Chem. Commun.*, 2017, **53**, 2024–2027.
31 H. Bunzen, Nonappa, E. Kalenius, S. Hietala and E. Kolehmainen, Subcomponent Self-Assembly: A Quick Way to New Metallogels, *Chem. - Eur. J.*, 2013, **19**, 12978–12981.
32 S. Ganta and D. K. Chand, Nanoscale metallogel via self-assembly of self-assembled trinuclear coordination rings: multi-stimuli-responsive soft materials, *Dalton Trans.*, 2015, **44**, 15181–15188.
33 (*a*) S. Dhibar, A. Dey, S. Majumdar, D. Ghosh, A. Mandal, P. P. Ray and B. Dey, A supramolecular Cd(II)-metallogel: an efficient semiconductive electronic device, *Dalton Trans.*, 2018, **47**, 17412–17420; (*b*) S. Dhibar, A. Dey, D. Ghosh, S. Majumdar, A. Dey, P. Mukherjee, A. Mandal, P. P. Ray, B. Dey and A. Supramolecular Gel, of Oxalic Acid-Monoethanolamine for Potential Schottky Barrier Diode Application, *ChemistrySelect*, 2019, **4**, 1535–1541; (*c*) S. Dhibar, A. Dey, S. Majumdar, A. Dey, P. P. Ray and B. Dey, Organic-Acid-Mediated Luminescent Supramolecular Tb(III)-metallogel Applied in an Efficient Photosensitive Electronic Device with Excellent Charge Transport Properties, *Ind. Eng. Chem. Res.*, 2020, **59**, 5466–5473; (*d*) S. Dhibar, A. Dey, S. Majumdar, P. P. Ray and B. Dey, Terephthalic acid-directed supramolecular Cu(II)-metallogel for photosensitive semiconducting Schottky diode with promising electronic charge transportation, *Int. J. Energy Res.*, 2021, **45**, 5486–5499.
34 W. Weng, X. Fang, H. Zhang, H. Peng, Y. Lin and Y. Chen, Multiresponsive supramolecular gels constructed by orthogonal metal–ligand coordination and hydrogen bonding, *Eur. Polym. J.*, 2013, **49**, 4062–4071.
35 K. Karmakar, A. Roy, S. Dhibar, S. Majumder, S. Bhattacharjee, B. Mondal, S. M. Rahaman, R. Saha, S. J. Ray and B. Saha, Instantaneous Gelation of a Self-Healable Wide-Bandgap Semiconducting Supramolecular Mg(II)-Metallohydrogel: An Efficient Nonvolatile Memory Design with Supreme Endurance, *ACS Appl. Electron. Mater.*, 2023, **5**, 3340–3349.
36 (*a*) S. Dhibar, D. Ghosh, S. Majumdar and B. Dey, Triethylenetetramine-Based Semiconducting Fe(III) Metallogel: Effective Catalyst for Aryl–S Coupling, *ACS Omega*, 2020, **5**, 2680–2689; (*b*) S. Dhibar, A. Dey, R. Jana, A. Chatterjee, G. K. Das, P. P. Ray and B. Dey, A semiconducting supramolecular Co(II)-metallohydrogel: an efficient catalyst for single-pot aryl–S bond formation at room temperature, *Dalton Trans.*, 2019, **48**, 17388–17394; (*c*) S. Dhibar, R. Jana, P. P. Ray and B. Dey, Monoethanolamine and Fe (III) based metallohydrogel: An efficient Schottky barrier diode, *J. Mol. Liq.*, 2019, **289**, 111126; (*d*) S. Dhibar, A. Dey, D. Ghosh, A. Mandal and B. Dey, Mechanically tuned molybdenum dichalcogenides (MoS_2 and $MoSe_2$) dispersed supramolecular hydrogel scaffolds, *J. Mol. Liq.*, 2019, **276**, 184–193; (*e*) D. Ghosh, S. Dhibar, A. Dey, S. Mukherjee, N. Joardar, S. P. Sinha Babu and B. Dey, Graphene oxide dispersed supramolecular hydrogel capped benign green silver nanoparticles for anticancer, antimicrobial, cell attachment and intracellular imaging applications, *J. Mol. Liq.*, 2019, **280**, 1–12.
37 H. Li, J. Zhang, H. Xue, L. Li, X. Liu, L. Yang, Z. Gu, Y. Cheng, Y. Li and Q. Huang, An injectable all-small-molecule dynamic

metallogel for suppressing sepsis, *Mater. Horiz.*, 2023, **10**, 1789–1794.

38 T. Feldner, M. Häring, S. Saha, J. Esquena, R. Banerjee and D. D. Díaz, Supramolecular Metallogel That Imparts Self-Healing Properties to Other Gel Networks, *Chem. Mater.*, 2016, **28**, 3210–3217.

39 S. Sarkar, S. Dutta, S. Chakrabarti, P. Bairi and T. Pal, Redox-switchable copper(I) metallogel: a metal-organic material for selective and naked-eye sensing of picric acid, *ACS Appl. Mater. Interfaces*, 2014, **6**, 6308–6316.

40 B. Xing, M.-F. Choi and B. Xu, Design of Coordination Polymer Gels as Stable Catalytic Systems, *Chem. - Eur. J.*, 2002, **8**, 5028–5032.

41 S. Saha, E.-M. Schon, C. Cativiela, D. D. Diaz and R. Banerjee, Proton-Conducting Supramolecular Metallogels from the Lowest Molecular Weight Assembler Ligand: A Quote for Simplicity, *Chem. – Eur. J.*, 2013, **19**, 9562–9568.

42 S. Saha, B. Pal, K. S. Das, P. K. Ghose, A. Ghosh, A. De, A. K. Das, P. P. Ray and R. Mondal, Design of Dual Purpose Fe-metallogel for Magnetic Refrigeration and Fabrication of Schottky Barrier Diode, *ChemistrySelect*, 2022, **7**, e202203307.

43 (*a*) S. Dhibar, S. K. Ojha, A. Mohan, S. P. C. Prabhakaran, S. Bhattacharjee, K. Karmakar, P. Karmakar, P. Predeep, A. K. Ojha and B. Saha, A multistimulus-responsive self-healable supramolecular copper(II)-metallogel derived from L-(+) tartaric acid: an efficient Schottky barrier diode, *New J. Chem.*, 2022, **46**, 17189–17200; (*b*) S. Dhibar, H. Dahiya, K. Karmakar, S. Kundu, S. Bhattacharjee, G. C. Nayak, P. Karmakar, G. D. Sharma and B. Saha, A transparent self-healable multistimuli-responsive novel supramolecular Co(II)-metallogel derived from adipic acid: Effective hole transport layer for polymer solar cells, *J. Mol. Liq.*, 2023, **370**, 121020; (*c*) S. Dhibar, A. Dey, A. Dalal, S. Bhattacharjee, R. Sahu, R. Sahoo, A. Mondal, S. M. Rahaman, S. Kundu and B. Saha, An organic acid consisted multiresponsive self-healing supramolecular Cu(II)-metallogel: Fabrication and analysis of semiconducting device, *J. Mol. Liq.*, 2023, **370**, 121021; (*d*) S. Dhibar, S. Babu, A. Mohan, G. K. Chandra, S. Bhattacharjee, K. Karmakar, P. Karmakar, S. M. Rahaman, P. Predeep and B. Saha, A novel citric acid facilitated supramolecular Zinc(II)-metallogel: Toward semiconducting device applications, *J. Mol. Liq.*, 2023, **375**, 121348; (*e*) K. Karmakar, A. Dey, S. Dhibar, R. Sahu, S. Bhattacharjee, P. Karmakar, P. Chatterjee, A. Mondal and B. Saha, A novel supramolecular Zn(II)-metallogel: an efficient microelectronic semiconducting device application, *RSC Adv.*, 2023, **13**, 2561–2569; (*f*) S. Dhibar, B. Pal, K. Karmakar, S. Kundu, S. Bhattacharjee, R. Sahoo, S. M. Rahaman, D. Dey, P. P. Ray and B. Saha, Exploring a supramolecular gel to *in situ* crystal fabrication from the low molecular weight gelators: a crystal engineering approach towards microelectronic device application, *ChemistrySelect*, 2023, **8**, e202204214.

44 X. Cheng, J. Pan, Y. Zhao, M. Liao and H. Peng, Gel Polymer Electrolytes for Electrochemical Energy Storage, *Adv. Energy Mater.*, 2018, **8**, 1702184.

45 K. Kumari, A. Kumar, D. K. Kotnees, J. Balakrishnan, A. D. Thakur and S. J. Ray, Structural and resistive switching behaviour in lanthanum strontium manganite-reduced graphene oxide nanocomposite system, *J. Alloys Compd.*, 2020, **815**, 152213.

46 (*a*) K. Kumari, A. Kumar, A. D. Thakur and S. J. Ray, Charge transport and resistive switching in a 2D hybrid interface, *Mater. Res. Bull.*, 2021, **139**, 111195; (*b*) A. Kumar, K. Kumari, S. J. Ray and A. D. Thakur, Graphene mediated resistive switching and thermoelectric behavior in lanthanum cobaltate, *J. Appl. Phys.*, 2020, **127**, 23.

47 K. Kumari, S. Majumder, A. D. Thakur and S. J. Ray, Temperature-dependent resistive switching behaviour of an oxide memristor, *Mater. Lett.*, 2021, **303**, 130451.

48 K. Kumari, A. D. Thakur and S. J. Ray, The effect of graphene and reduced graphene oxide on the resistive switching behavior of $La_{0.7}Ba_{0.3}MnO_3$, *Mater. Today Commun.*, 2021, **26**, 102040.

49 K. Kumari, S. Kar, A. D. Thakur and S. J. Ray, Role of an oxide interface in a resistive switch, *Curr. Appl. Phys.*, 2022, **35**, 16–23.

50 N. Alam, S. Majumder, S. J. Ray and D. Sarma, A Wide Bandgap Semiconducting Magnesium Hydrogel: Moisture Harvest, Iodine Sequestration, and Resistive Switching, *Langmuir*, 2022, **38**, 10601–10610.

51 A. Bhakat, S. Sen, S. Banerjee and K. Sarkar, Plant growth promotion and lipopeptide-mediated biological control of chilli pathogen Colletotrichum siamense by endophytic Bacillus sp, *Physiol. Mol. Plant Pathol.*, 2023, **125** 102026.

52 S. Banerjee, S. Sen, A. Bhakat, A. Bhowmick and K. Sarkar, The lipopeptides fengycin and iturin are involved in the anticandidal activity of endophytic Bacillus sp. as determined by experimental and in silico analysis, *Lett. Appl. Microbiol.*, 2022, **75**, 450–459.

53 A. Ghosh, S. K. Dubey, M. Patra, J. Mandal, N. N. Ghosh, P. Das and S. Bhattacharjee, Solvent- and Substrate-Induced Chiroptical Inversion in Amphiphilic, Biocompatible Glycoconjugate Supramolecules: Shape-Persistent Gelation, Self-Healing, and Antibacterial Activity, *Chem. – Eur. J.*, 2022, **28**, e202201621.

54 W. Chu, Y. Yang, J. Cai, H. Kong, M. Bai, X. Fu, S. Qin and E. Zhang, Synthesis and Bioactivities of New Membrane-Active Agents with Aromatic Linker: High Selectivity and Broad-Spectrum Antibacterial Activity, *ACS Infect. Dis.*, 2019, **5**, 1535–1545.

55 K. Flemming, C. Klingenberg, J. P. Cavanagh, M. Sletteng, W. Stensen, J. S. Svendsen and T. Flægstad, High in vitro antimicrobial activity of synthetic antimicrobial peptidomimetics against staphylococcal biofilms, *J. Antimicrob. Chemother.*, 2009, **63**, 136–145.

56 H. Zhang, X. Sun, J. Wang, Y. Zhang, M. Dong, T. Bu, L. Li, Y. Liu and L. Wang, Multifunctional Injectable Hydrogel Dressings for Effectively Accelerating Wound Healing: Enhancing Biomineralization Strategy, *Adv. Funct. Mater.*, 2021, **31**, 2100093.

57 J. Chen, J. He, Y. Yang, L. Qiao, J. Hu, J. Zhang and B. Guo, Antibacterial adhesive self-healing hydrogels to promote diabetic wound healing, *Acta Biomater.*, 2022, **146**, 119–130.
58 I. P. Sæbø, M. Bjørås, H. Franzyk, E. Helgesen and J. A. Booth, Optimization of the Hemolysis Assay for the Assessment of Cytotoxicity, *Int. J. Mol. Sci.*, 2023, **24**, 2914.
59 S. Taritla, M. Kumari, S. Kamat, S. G. Bhat and C. Jayabaskaran, Optimization of PhysicoChemical Parameters for Production of Cytotoxic Secondary Metabolites and Apoptosis Induction Activities in the Culture Extract of a Marine Algal–Derived Endophytic Fungus *Aspergillus* sp, *Front. Pharmacol.*, 2021, **12**, 1–18.